

# Spatially Selective Radar Backscatter Communication

## Abstract

This paper presents Serena, the first *spatially selective* radar backscatter communication system that is capable of delivering messages to radars at specific locations. Rather than manipulating RF signals with power-intensive components, Serena leverages the limited modulation capability of multiple low-power backscatter tags to generate spatially selective radar signal feature, and further utilizes such signal feature to represent bits. Such design philosophy is primarily realized by our two core designs: (i) a multi-tag distributed and synchronous modulation technique that generates spatially selective radar signal feature (i.e., the combination of the frequencies of tag-generated harmonics in radar IF spectrum); (ii) an intermittent mutual synchronization protocol that achieves  $10\text{-}\mu\text{s}$  level inter-tag synchronization under only  $10\mu\text{W}$ -level power consumption. Our extensive experiments demonstrate that Serena achieves desirable spatial selectivity in diverse environments: it achieves *less than 1% average BER* at target locations, while keeping the average BER around 30% at non-target locations. Serena offers a low-power solution for delivering location-specific messages to radar-equipped automobile, UAV, and UGV.

## 1 Introduction

**Motivation.** Recent years have witnessed the rapid development of radar backscatter communication [1–7], a technology that sends bits to radar by modulating and reflecting radar signal using backscatter tag. It is envisionable that such technology is a promising enabler of *ubiquitous message delivery to vehicles*. In contrast to power-hungry and bulky roadside units and base stations, low-power and compact backscatter tags can be flexibly deployed in challenging environments with limited communication infrastructures (e.g., remote wilderness, rural highway, underground mine). Moreover, miniature radars have already been widely equipped by today’s vehicles: reportedly, over 85 million vehicular radars [8] were deployed world-wide in the year of 2024 alone.

Though promising, existing radar backscatter communication systems still lack a necessary ability of *spatial selectivity* (i.e., selectively sending messages to radars at specific locations). The necessity of such ability stems from the location-specific nature of vehicle-destined messages in a number of real-world scenarios: a no-fly-zone (NFZ) alert should be sent to the unmanned aerial vehicles (UAVs) in the restricted airspace of a wildlife sanctuary; a speed-reduction warning should be sent to the automobiles in the under-construction lane of a rural highway at a safety distance from the construction site; a turning notification should be sent to the

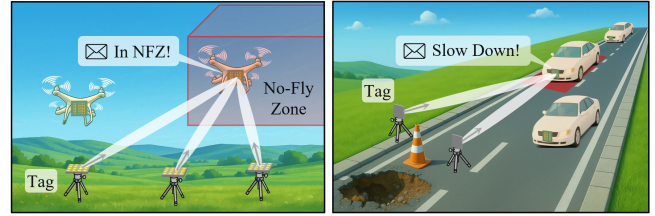


Figure 1: Examples of Serena applications (target location in red). unmanned ground vehicles (UGVs) meters away from the turning area in an underground mine tunnel.

Unfortunately, existing radio frequency (RF) spatially selective communication methods [9–13] are inapplicable in the context of radar backscatter. Specifically, they employ beamforming to concentrate RF signals at the target location, which requires RF transmitter to accurately and flexibly manipulate various RF signal properties (e.g., phase, frequency, amplitude) with power-intensive components (e.g., phase shifter, VCO, amplifier) consuming W-level power in total. Such excessive power consumption far exceeds the stringent power budget ( $m\text{W}$ -level or below) of radar backscatter tag.

**Philosophy.** This paper proposes Serena<sup>1</sup>, the first system that enables spatially selective radar backscatter communication with low-power tags. Serena avoids manipulating the spatial distribution of RF signal strength, but leverages the limited modulation capability of *low-power* backscatter tags to generate *location-specific* and *tag-controllable* feature in the spectrum of radar intermediate frequency (IF) signal, and further utilizes such feature to represent bits. It is such design philosophy that empowers Serena with spatial selectivity, as it helps ensure that valid packets (those with valid preambles and correct payloads) only appear at target locations, whereas at non-target locations only invalid packets appear.

**Core Challenges & Designs.** Realizing such philosophy faces two fundamental challenges C1 and C2. We elaborate on them and the designs of Serena that address them.

**C1: Limited Single-Tag Impact on IF Signal.** The core of radar backscatter communication is to exploit the harmonics induced by backscatter tags in radar IF signal to represent bits. However, it is rather difficult for a single tag to induce harmonics that carry location-specific features. Specifically, a single tag induces either Doppler or range harmonics (Fig. 2b–2c): the former correlate with velocity which are intrinsically location-independent; the latter correlate with radar-tag distance which only partially characterizes the radar location.

Serena addresses C1 by shifting from existing single-tag independent modulation to multi-tag *harmonic-division distributed (HDD)* modulation. Specifically, HDD modulation

<sup>1</sup>Serena comes from Spatially selective radar backscatter communication.

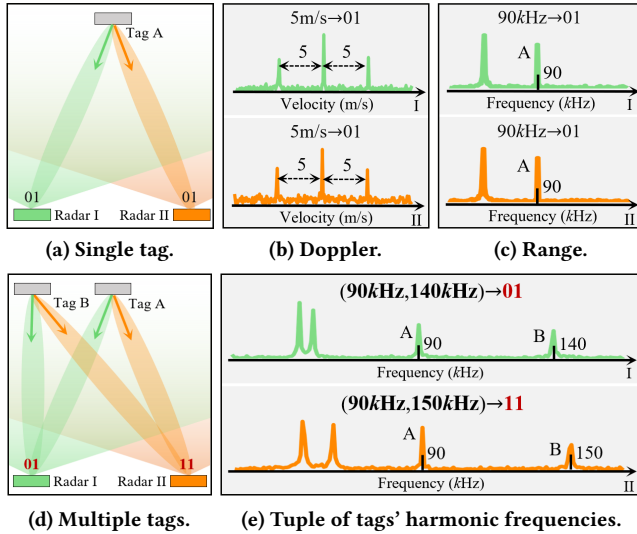


Figure 2: Comparison between existing methods (a: single-tag system architecture; b-c: exploited harmonic) and Serena (d: multi-tag system architecture; e: exploited feature).

employs multiple backscatter tags to synchronously perform FSK on incident radar chirps, and utilizes the tuple comprising the frequency of the (first) harmonic that each tag generates in radar IF spectrum to represent bits (Fig. 2e). Such tuple is location-specific: given tags' modulation frequencies, the tuple differs across different radar locations, because it is decided by the distances from the radar to multiple tags, which uniquely pinpoint a location within tags' radiation coverage. Such tuple is also tag-controllable: each element in the tuple is controlled by the modulation frequency of the corresponding tag. Empowered by such attributes, HDD modulation sets tags' modulation frequencies to ensure that the harmonic frequency tuple that corresponds to the bits to be delivered only appears at the target location.

*C2: Synchronization under Strict Power Budget.* Inter-tag synchronization is indispensable for Serena, as its HDD modulation requires tags to perform modulation in a synchronous manner. However, a radar backscatter tag usually has only  $mW$ -level or below power budget. Excluding the inevitable power consumption of modulating radar chirps, the power budget left for synchronization could be as little as  $100\mu W$ -level. Such strict power budget rules out any synchronization method that requires power-intensive on-tag components, including the most intuitive one that directly utilizes incident radar signal as synchronization reference, as such method requires to integrate with each tag  $100mW$ -level always-on components (e.g., LNA) for reliable radar signal detection.

Serena addresses C2 by integrating with each tag a synchronization radio, and letting the tags follow an *intermittent mutual synchronization protocol*. Specifically, the protocol lets one tag broadcast synchronization packets, and the others align their local clocks with that of the broadcasting

tag. Moreover, the protocol keeps each tag's synchronization radio sleeping for most of the time and activates it only when necessary. Such intermittent operation enables each tag of Serena to achieve synchronization with only  $10\mu W$ -level power consumption, even if its synchronization radio is implemented with  $10mW$ -level commercial-off-the-shelf radio chip, eliminating the necessity of developing active radio hardware under the  $100\mu W$ -level power budget.

**Contributions.** This paper has the following contributions in terms of functionality, design, and implementation.

- *Functionality.* This paper proposes Serena, the first system that empowers radar backscatter communication with spatial selectivity by enabling low-power backscatter tags to generate location-specific and tag-controllable feature in the spectrum of radar IF signal. Serena offers a low-power solution for delivering location-specific messages to radar-equipped automobile, UAV, and UGV.
- *Design.* Serena contains a series of customized designs: (i) a harmonic-division distributed modulation technique that employs multiple backscatter tags to synchronously perform FSK on incident radar chirps, and uses the frequencies of the tag-generated harmonics in radar IF spectrum to represent bits, (ii) an intermittent mutual synchronization protocol that achieves  $10\mu s$ -level inter-tag synchronization with only  $10\mu W$ -level power consumption, and (iii) extended designs, including an augmented modulation technique that realizes message delivery to target region comprising a continuum of locations, and many others.
- *Implementation.* This paper implements two types of radar backscatter tags compatible with 24GHz FMCW mmWave radar, whose differentiated antenna gains and radiation coverages enable Serena to operate in diverse real-world environments. This paper conducts extensive experiments to evaluate Serena's performance in 1-D line, 2-D plane, and 3-D space. The experimental results validate that Serena achieves desirable spatial selectivity with *less than 1% average bit error rate (BER)* at target locations and around 30% BER at non-target locations, and is robust against diverse practical factors, including mutual radar interference, radar orientation, and radar speed.

## 2 Overview of Serena

**Core Design Principle.** The core design principle of Serena is to utilize the *frequencies of tag-generated harmonics to represent bits*. Specifically, a radar backscatter tag that performs FSK modulation on incident radar chirp will generate a (first) harmonic in radar IF signal [6] whose frequency  $h$  satisfies the following Eq. (1),

$$h = \frac{LR}{c} + f, \quad (1)$$

where  $L$  is twice of the radar chirp slope,  $R$  is the tag-radar distance,  $c$  is the speed of light in the air, and  $f$  is the tag

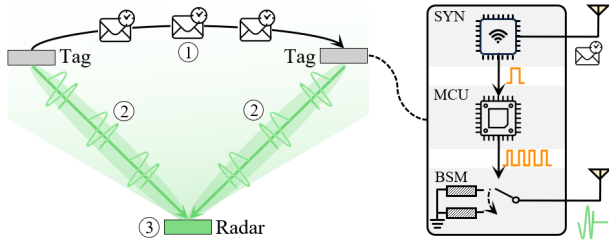


**Figure 3: Serena’s workflow** (①: synchronization; ②: modulation; ③: demodulation) and hardware components (SYN: synchronization radio; MCU: microcontroller unit; BSM: backscatter module).

modulation frequency. We hereafter refer to the first harmonic simply as harmonic. Such harmonic frequency enjoys the properties of location specificity and tag controllability (whose detailed rationales are provided in Appendix A).

- **Location Specificity.**  $K \in \{1, 2, 3\}$  radar backscatter tags performing FSK with fixed modulation frequencies generate a unique tuple of harmonic frequencies at each location in  $K$ -dimensional space within tags’ radiation coverage.
- **Tag Controllability.** A radar backscatter tag that performs FSK modulation can control the harmonic frequency generated by it via adjusting its modulation frequency.

Empowered by such attributes, Serena sets tags’ modulation frequencies to ensure spatial selectivity in principle: valid packets only appear at target locations, whereas only invalid packets appear at non-target locations.

**Hardware Components.** As shown in Fig. 3, the hardware components of Serena deployed in real-world environments consist of multiple radar backscatter tags which communicate with radar in a spatially selective manner. Specifically, each tag constitutes a backscatter module, an MCU, and a synchronization radio: the backscatter module consists of an antenna to receive and reflect radar chirps, as well as a modulation unit (RF switch or diode); the MCU generates the square wave to control the modulation unit; the synchronization radio consists of an antenna and a radio chip to transmit or receive synchronization packets, and is connected to the GPIO port of the MCU, through which it conveys pulse signals to calibrate the tag’s local clock. The radar side executes Serena’s light-weight demodulation technique.

**Workflow.** The workflow of Serena consists of both the pre-deployment process and the post-deployment process (as illustrated in Fig. 3) discussed as follows.

**Pre-Deployment Process.** Before deployment, Serena’s modulation technique constructs a mapping from the tuple of tags’ harmonic frequencies to the represented symbol, and generates the configurations of each tag’s modulation frequencies and timings based on the constructed mapping, the target location, as well as the symbols to be delivered. Such configurations are stored in each tag’s MCU. When the target locations change, such configurations can be updated via the over-the-air configuration method elaborated in § 7.

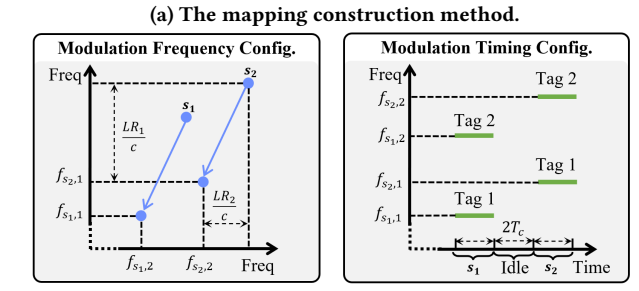
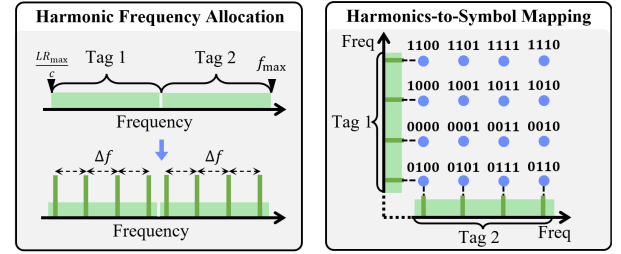


**Figure 4: HDD modulation** ( $X = 2$ ,  $N = 4$ ,  $M = 4$ ,  $s_1 = 1001$ ,  $s_2 = 1110$ ).

**Post-Deployment Process.** Upon deployment, the tags periodically synchronize their local clocks via Serena’s synchronization technique. After the first synchronization event, the tags begin to modulate radar chirps according to the stored modulation configurations, and calibrate their clocks after each subsequent synchronization event.

### 3 Modulation & Demodulation Techniques

#### 3.1 HDD Modulation

Harmonic-division distributed (HDD) modulation consists of mapping construction and modulation configuration.

**Mapping Construction.** This method takes the number of tags  $X$  and the interval  $\Delta f$  between adjacent candidate harmonic frequencies of a tag as inputs, and outputs a one-to-one mapping from the tuple of harmonic frequencies generated by different tags to the represented symbol. As shown in Fig. 4a, this method consists of the following two steps.

- **Step 1 (Harmonic Frequency Allocation).** This step selects  $(\frac{LR_{\max}}{c}, f_{\max})$  as the overall candidate frequency band for tags’ harmonics, where  $R_{\max}$  is the maximum radar-tag distance for a radar to robustly detect tag-generated harmonics, and  $f_{\max}$  is the maximum frequency of radar IF signal. This step then equally divides the overall candidate frequency band into  $X$  non-overlapping sub-bands, each allocated to a distinct tag. This step finally selects from each sub-band the maximum possible number  $N$  of discrete frequencies as the candidate harmonic frequencies, with each two adjacent frequencies separated by  $\Delta f$ .
- **Step 2 (Harmonics-to-Symbol Mapping).** This step constructs a set  $\mathcal{F}$  consisting of  $N^X$  tuples, where each tuple consists of  $X$  elements with each element being a candidate harmonic frequency (selected in step 1) of a tag. This

step then constructs the set  $\mathcal{F}_M \subseteq \mathcal{F}$ , where  $\mathcal{F}_M$  consists of  $2^M$  elements in  $\mathcal{F}$  with  $M$  being the largest integer such that  $2^M \leq N^X$ . Finally, this step constructs a one-to-one mapping  $\phi(\cdot)$  from  $\mathcal{F}_M$  to the set  $\mathcal{S}$  consisting of all the binary symbols of length  $M$ , such that the mapped symbols for two adjacent tuples in  $\mathcal{F}_M$  differ by only one bit.

**Modulation Configuration.** As illustrated in Fig. 4b, given the constructed mapping  $\phi(\cdot)$ , the target location, and the message that the tags aim to deliver to the target location, this method configures each tag's modulation frequency and timing in the following two steps to deliver such message.

- **Step 1 (Modulation Frequency Configuration).** This step first segments the message into a set  $\mathcal{M} \subseteq \mathcal{S}$  of symbols. For each symbol  $s \in \mathcal{M}$ , this step then sets the tuple  $(h_{s,1}, h_{s,2}, \dots, h_{s,X}) = \phi^{-1}(s)$ , where  $h_{s,i}$  is the harmonic frequency that tag  $i$  should generate at the target location to deliver  $s$ . This step then configures the modulation frequency  $f_{s,i}$  of each tag  $i$  as  $f_{s,i} = h_{s,i} - \frac{LR_i}{c}$  by Eq. (1), where  $R_i$  is the distance between the target location and tag  $i$ .
- **Step 2 (Modulation Timing Configuration).** As shown in Fig. 4b, to deliver each symbol  $s \in \mathcal{M}$ , the  $X$  tags synchronously perform FSK for  $2T_c$  with modulation frequencies  $(f_{s,1}, f_{s,2}, \dots, f_{s,X})$  computed in step 1 where  $T_c$  denotes chirp duration. This step assigns a  $2T_c$  idle duration between the modulations for two consecutive symbols.

### 3.2 Properties of HDD Modulation

HDD modulation enjoys the following desirable properties.

**Property 1.** *The modulation duration  $2T_c$  specified in HDD modulation is the shortest duration that ensures an integral chirp is modulated for each symbol.*

**Rationale of Property 1.** As a low-power backscatter tag lacks the necessary power-intensive components (e.g., LNA) to reliably detect radar chirps, it cannot align the start time of its modulation with that of an incident chirp. As a result, each tag's modulation duration should be no less than  $2T_c$  to ensure that at least one chirp is integrally modulated for each symbol. We illustrate such fact with the experiment shown in Fig. 5a, where we configure an TinyRad [14] mmWave radar to transmit a series of chirps, a Serena tag to modulate and reflect the chirps, an ADL6010 [15] mmWave envelope detector (mmED) to detect the chirps, and an oscilloscope to collect the output of mmED and the tag's modulation control signal to obtain the ground truths of modulation and chirp timings. As shown in Fig. 5b,  $2T_c$  modulation duration ensures that one chirp is integrally modulated for each symbol; when modulation duration decreases (e.g.,  $T_c$ ), there could be no integrally modulated chirp for some symbol. The necessity of modulating an integral chirp is that the harmonic strength of a tag is proportional to the square of the duration for which a chirp is modulated by it, as shown in Fig. 5c.

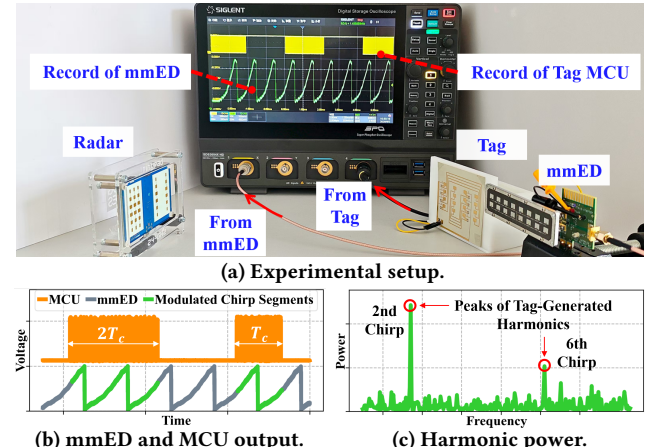


Figure 5: Experiment demonstrating property 1 of HDD modulation.

**Property 2.** *The idle duration  $2T_c$  specified in HDD modulation is the shortest duration that ensures an integral chirp is unmodulated between two consecutive symbols.*

**Rationale of Property 2.** The idle interval should be no less than  $2T_c$  to ensure that at least an integral chirp is unmodulated between two consecutive symbols. Leaving integrally unmodulated chirp enables the radar side to estimate the environmental interference in the spectrum of IF signal, such that the demodulation method running at the radar side can eliminate environmental interference. Detailed environmental elimination process is given in § 3.3.

**Property 3.** *HDD modulation constructs the largest symbol set that supports message delivery to any location whose distance to each tag is no greater than  $R_{\max}$ .*

**Rationale of Property 3.** Such property holds for three reasons. First, HDD modulation selects as many candidate frequencies as possible in the overall candidate frequency band  $(\frac{LR_{\max}}{c}, f_{\max})$ . Second, if another candidate frequency  $f'$  is added to represent more symbols,  $f'$  must come from the range  $(0, \frac{LR_{\max}}{c}]$ . As a result, it is impossible for a tag to manipulate its modulation frequency  $f$ , such that its harmonic frequency  $f + \frac{LR_{\max}}{c} > \frac{LR_{\max}}{c}$  equals to the added candidate frequency  $f' \leq \frac{LR_{\max}}{c}$  at the target location with a distance of  $R_{\max}$  to the tag. Third, for any frequency  $f'' \in (\frac{LR_{\max}}{c}, f_{\max})$ , a tag can manipulate its modulation frequency  $f$  such that its harmonic frequency  $f + \frac{LR}{c} = f''$  at any location whose distance  $R$  to the tag satisfies  $R \leq R_{\max}$ . Consequently, HDD modulation constructs the largest set of symbol-representing frequency tuples, resulting in the largest symbol set. It is notable that property 3 contributes to improving the data rate.

### 3.3 HDD Demodulation

Now, we introduce Serena's HDD demodulation technique.

**Demodulation Technique.** For each chirp  $j$  that the radar receives, the radar side computes the spectrum of its IF

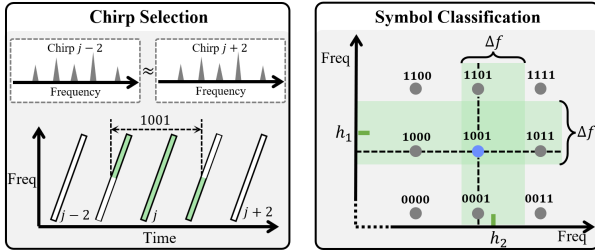


Figure 6: Step 1 and 3 of HDD demodulation (same setting as Fig. 4; chirp  $j$  is modulated by tag 1 and tag 2 to carry symbol 1001).

signal, and those of chirp  $j - 2$  and  $j + 2$  received  $2T_c$  before and after it. Next, the radar side inputs the three spectra, as well as  $\Delta f$  and  $X$  into the HDD demodulation method, which consists of the following three steps.

- **Step 1 (Chirp Selection).** As shown in Fig. 6, if the IF spectra of chirp  $j - 2$  and  $j + 2$  are nearly identical, this step regards chirp  $j$  as integrally modulated by the tags and selects it. Otherwise, the demodulation process is terminated.
- **Step 2 (Harmonic Retrieval).** This step subtracts the IF spectrum of chirp  $j - 2$  from that of chirp  $j$  to obtain an interference-suppressed IF spectrum, in which this step selects the peak with the highest amplitude from each tag  $i$ 's allocated frequency band, and sets the frequency  $h_i$  of such peak as the observed harmonic frequency of tag  $i$ .
- **Step 4 (Symbol Classification).** As shown in Fig. 6, if there exists a symbol  $s$  such that  $h_{s,i} \in (h_i - \frac{\Delta f}{2}, h_i + \frac{\Delta f}{2})$  holds for each tag  $i$ , where  $(h_{s,1}, h_{s,2}, \dots, h_{s,X}) = \phi^{-1}(s)$ , this step outputs  $s$ . Otherwise, no output is produced.

**Rationale.** The rationale of step 1 lies in that if chirp  $j$  is integrally modulated by the tags, the IF spectra of chirp  $j - 2$  and  $j + 2$  are nearly identical, because they are both unmodulated chirps, which typically does not hold if chirp  $j$  is not integrally modulated. The rare exceptional case and method to deal with it are given in Appendix B. The rationale of step 2 lies in that the IF spectrum of the unmodulated chirp  $j - 2$  provides a faithful estimate of environmental interference. Note that step 3 will not output more than one symbol, which is ensured by the  $\Delta f$  spacing between any two adjacent symbol-representing harmonic frequencies of each tag. Furthermore, although HDD demodulation technique demodulates a chirp  $2T_c$  after the radar receives it, such delay is negligible because  $T_c$  is only  $100\mu\text{s}$ - to  $1\text{ms}$ -level.

### 3.4 Spatially Selective Resolution

Having introduced the modulation and demodulation techniques of Serena, we now carry out a detailed discussion of its spatially selective capability. We measure such capability with *spatially selective resolution (SSR)*, which is the precision of the target location where messages could be delivered.

**SSR Result.** The SSR of Serena is negatively correlated with  $\Delta f$  and positively correlated with  $X$ .

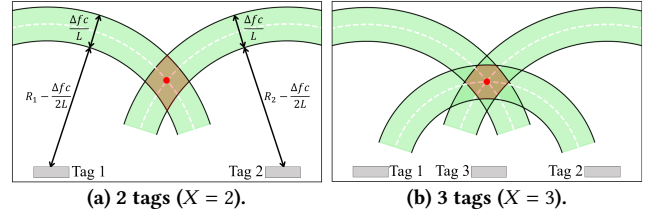


Figure 7: Illustration of Serena's spatially selective resolution (red dot: target location; orange space: cell formed by realized locations).

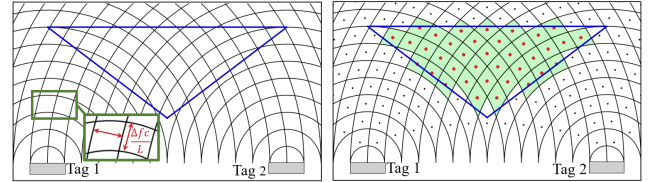


Figure 8: Illustration of step 1 and 2 of HDD<sup>+</sup> modulation (blue triangle: target region; green cell: internal cell).

**SSR Analysis.** According to § 3.1, to deliver a symbol  $s$  to the target location, each tag  $i$  modulates at frequency  $f_{s,i} = h_{s,i} - \frac{R_i L}{c}$ , where  $(h_{s,1}, h_{s,2}, \dots, h_{s,X}) = \phi^{-1}(s)$ , and  $R_i$  is the distance between the target location and tag  $i$ . Clearly, for any location  $p$ , the harmonic frequency of tag  $i$  at  $p$  is  $h_i = h_{s,i} - \frac{R_i L}{c} + \frac{R_{p,i} L}{c}$  according to Eq. (1), where  $R_{p,i}$  is the distance between  $p$  and tag  $i$ . If the radar side could demodulate  $s$  at  $p$ , then according to the demodulation method in § 3.3,

$$h_{s,i} - \frac{\Delta f}{2} < h_{s,i} - \frac{R_i L}{c} + \frac{R_{p,i} L}{c} < h_{s,i} + \frac{\Delta f}{2} \quad (2)$$

holds for each tag  $i$ . We reorganize Inequality (2) and obtain the following Inequality (3),

$$R_i - \frac{\Delta f c}{2L} < R_{p,i} < R_i + \frac{\Delta f c}{2L}, \quad (3)$$

which specifies the constraints on the distance from each tag  $i$  to the location  $p$  where symbol  $s$  is actually delivered. We call one such location  $p$  a *realized (communication) location*.

Inequality (3) indicates that when  $\Delta f \rightarrow 0$ , we have  $R_{p,i} \rightarrow R_i$ , and the realized locations converge to the target location; when  $\Delta f$  is a positive value, the realized locations form a continuum of space, referred to as a *cell*, with the target location at the center. As shown in Fig. 7, in 2-D space, a cell spans the intersection of multiple annuluses of width  $\frac{\Delta f c}{L}$ . Clearly, smaller  $\Delta f$  increases SSR by imposing stricter constraints in Inequality (3); larger  $X$  increases SSR by adding constraints in the form of Inequality (3) as shown in Fig. 7.

### 3.5 HDD<sup>+</sup> Modulation & Demodulation

As introduced in § 3.4, HDD modulation and demodulation enable Serena to deliver messages to a cell. Now, we introduce HDD<sup>+</sup> modulation and demodulation, which enable message delivery to a target *region* comprising multiple cells. Note that HDD<sup>+</sup> and HDD demodulation are the same, and the following discussions focus on HDD<sup>+</sup> modulation.

**HDD<sup>+</sup> Modulation in 2-D Space.** HDD<sup>+</sup> modulation consists of a mapping construction and a modulation configuration method. The mapping construction method is the same with that of HDD modulation, which takes  $\Delta f$  and  $X$  as inputs, and constructs a harmonics-to-symbol mapping  $\phi(\cdot)$ . The modulation configuration method takes as inputs  $\phi(\cdot)$ ,  $X$ , the 2-D target region, as well as the message to be delivered, and proceeds in the following four steps.

- **Step 1 (Spatial Mesh Construction).** As illustrated in Fig. 8a, this step constructs multiple concentric circles centered at each tag  $i$ , whose radii span the set<sup>2</sup>  $\{\frac{m\Delta f c}{L} : m \in \mathbb{N}^+, m \leq \lfloor \frac{R_{\max} L}{\Delta f c} \rfloor\}$ . The intersected circles form a spatial mesh consisting of multiple cells in 2-D plane.
- **Step 2 (Internal Cell Identification).** As illustrated in Fig. 8b, this step identifies a cell as an internal cell if the mean coordinate of its vertices lies within the target region.
- **Step 3 (Modulation Frequency Configuration).** This step first segments the message into a set of symbols. To deliver each symbol  $s$  of the message to each internal cell  $k$ , this step sets the modulation frequency  $f_{s,i}^k$  of each tag  $i$  as

$$f_{s,i}^k = h_{s,i} - \frac{L}{c} \left( R_{k,i} + \frac{\Delta f c}{2L} \right) = h_{s,i} - \frac{R_{k,i} L}{c} - \frac{\Delta f}{2}, \quad (4)$$

where  $(h_{s,1}, h_{s,2}, \dots, h_{s,X}) = \phi^{-1}(s)$  and  $R_{k,i}$  is the inner radius of the annulus centered at tag  $i$  that forms cell  $k$ .

- **Step 4 (Modulation Timing Configuration).** This step iteratively delivers each symbol  $s$  of the message to each cell  $k$  by setting all tags to synchronously perform FSK for  $2T_c$  with modulation frequencies  $(f_{s,1}^k, f_{s,2}^k, \dots, f_{s,X}^k)$  computed in step 3. Besides, this step sets a  $2T_c$  idle interval between the modulations of two consecutive cells and symbols.

**HDD<sup>+</sup> Modulation in 1-D and 3-D Spaces.** HDD<sup>+</sup> modulation in 1-D and 3-D spaces are the same with that in 2-D space except that a cell takes the form of a line segment in 1-D space and a volumetric region in 3-D space.

## 4 Synchronization Protocol

### 4.1 Protocol Design

**Overview.** As shown in Fig. 9, Serena follows an *intermittent mutual (IM) sync*<sup>3</sup> protocol, where one tag serves as the sync master whose sync radio broadcasts sync packets, while the other tags act as sync slaves that receive such packets and align their local clocks with that of the sync master. Both the sync master and slaves operate in alternating states of executing sync operations (EXE) and sleeping (SLP).

**Details.** The details of the IM sync protocol are as follows.

**Sync Master.** When the sync master is powered up, it enters EXE. In EXE, it first transmits  $Y$  sync packets, among which each packet  $y$  is transmitted at a predefined local time  $t_y$

<sup>2</sup>Note that  $\lfloor \frac{R_{\max} L}{\Delta f c} \rfloor$  is the smallest integer that makes  $\frac{m\Delta f c}{L} \geq R_{\max}$ .

<sup>3</sup>Note that the term synchronization is abbreviated as *sync* hereafter.

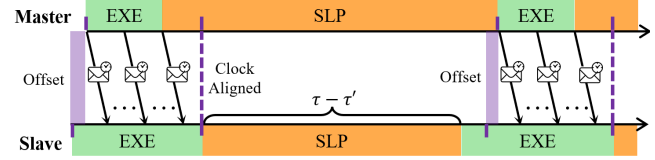


Figure 9: IM sync protocol (2-tag case).

with its payload set as the timestamp  $t_y$ . After that, the sync master sets a countdown timer that lasts for duration  $\tau$ , and enters SLP, during which it is deactivated to save power. When the timer expires, the sync master reenters EXE.

**Sync Slave.** When a sync slave is powered up, it enters EXE. In EXE, upon receiving each sync packet  $y$ , the sync slave reads its payload  $t_y$ , records the current time  $t'_y$  of its local clock, and computes the offset  $\Delta t$  between its local clock and that of the sync master as  $\Delta t = t_y - t'_y + \tau_c$  where  $\tau_c$  is a constant that accounts for transmission and propagation delays of a sync packet. After a predefined duration  $\tau'$  since the sync slave receives the first sync packet, it adjusts its local clock to align with that of the sync master based on the average offsets in current EXE, sets a countdown timer lasting for  $\tau - \tau'$ , and enters SLP. When the timer expires, the sync slave reenters EXE.

**Sync Packet.** Each of the transmitted sync packets takes the simplest format, which consists of only the indispensable preamble, sync master address, CRC bits, and a one-byte payload that contains the timestamp of the sync master.

### 4.2 Properties of IM Sync Protocol

**Property 1.** *The IM sync protocol suppresses the average power consumption of each tag’s sync radio to only 10μW-level even if it is realized using 10mW-level commercial radio chip.*

**Rationale of Property 1.** A core design of the IM sync protocol is to activate the sync radio only when necessary. Such intermittent operation enables the sync radio to consume only 10μW-level average power, even if it is realized with 10mW-level radio chip. Specifically, Serena sets  $\tau=5s$ , and adopts nRF52832 [16] as its sync radio, which enjoys tens-of-meters communication distance while consuming around 17mW power. The duration of EXE is around 10ms for sync master, and 10~20ms for sync slave. As illustrated in Fig. 10, the measured power of the sync master is around 45μW in SLP and 17.4mW in EXE. The duty cycle of the sync radio is  $\frac{10ms}{10ms+5s} = \frac{1}{501}$ . Consequently, the average power consumption of the sync master is  $\frac{500}{501} \times 45\mu W + \frac{1}{501} \times 1740\mu W \approx 48.4\mu W$ . Similarly, the average power consumption of the sync slave is  $48.5\mu W \sim 52.1\mu W$ . Note that Property 1 makes it unnecessary to develop new ultra-low power active radio hardware that meets a tag’s 100μW-level power budget.

**Property 2.** *The IM sync protocol ensures that the sync failure probability is below  $10^{-9}$ .*

**Rationale of Property 2.** The event of sync failure happens when a sync slave fails to receive any sync packet in

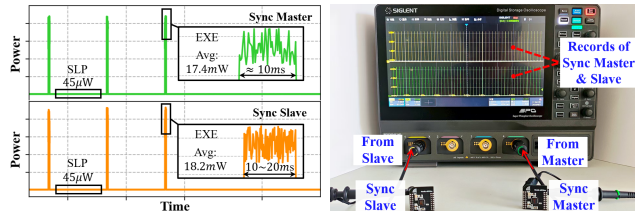


Figure 10: Power measurement. Figure 11: Offset measurement.

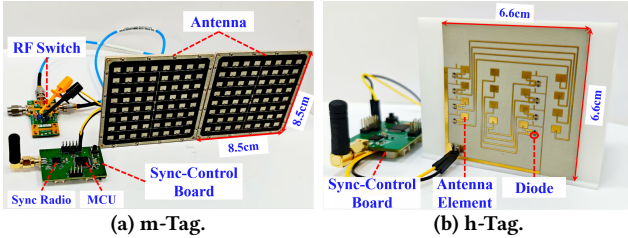


Figure 12: Radar backscatter tag prototypes of Serena.

one EXE. Our measurements in both indoor and outdoor environments show that a sync slave has an empirical failure probability of 3.5% to 13% for receiving one sync packet, which is primarily caused by the co-channel interference between nRF52832 and other Bluetooth radios. Consequently, the IM sync protocol sets  $Y = 10$ , which is the minimum number that ensures a below  $10^{-9}$  sync failure probability.

**Property 3.** *The IM sync protocol ensures that the master-slave clock offset is only 10 $\mu$ s-level.*

**Rationale of Property 3.** Such property is guaranteed by our proper selection of the SLP duration  $\tau$ . Specifically, the frequency error between the local clocks (i.e., crystal oscillators) of the sync master and a sync slave is around 10ppm. Thus, the IM sync protocol sets  $\tau = 5$ s to ensure the cumulative clock offset between two EXE states is smaller than 50 $\mu$ s. We also conduct experiment to evaluate the empirical master-slave clock offset. The setup of the experiment is illustrated in Fig. 11. Specifically, an oscilloscope is connected to the GPIO ports of the sync master and slave, which is configured to simultaneously generate rising-edge pulses via their GPIO ports at predefined timestamps. We collect the clock offset between the pulses, which is identical to that between sync master and slave. The experiment demonstrates that such clock offset is persistently lower than 49 $\mu$ s.

## 5 Performance Evaluation

This section evaluates Serena’s performance. All experiments have followed the standard procedures of IRB of our institute.

### 5.1 Implementation

**Tag.** This paper implements two kinds of radar backscatter tags, namely m-tag and h-tag, introduced as follows.

**m-Tag.** Inspired by [1], this paper builds the m-tag shown in Fig. 12a, consisting of an ADRF5026 [17] RF switch, two 24GHz microstrip array (MA) antennas connected to the RFC

and RF1 ports of the switch, as well as a sync-control board designed by this paper. The sync-control board consists of an nRF52832 [16] radio chip as the sync radio, and a STM32L4 [18] MCU that controls the RF switch. Although nRF52832 is also capable of generating control signals, it is only used as sync radio and is set to sleep for most of the time, because its running power consumption is significantly higher than that of STM32L4 (only 515 $\mu$ W at 4MHz clock frequency set by this paper). The power consumption of m-tag is around 910 $\mu$ W (570 $\mu$ W from the sync-control board and 340 $\mu$ W from the RF switch). The MA antennas provide a gain of 22dBi, and their radiation coverage is around 10° in both azimuth and elevation planes. Such strong gain and narrow radiation pattern motivate us to use m-tag in 1-D experiments.

**h-Tag.** This paper builds the h-tag shown in Fig. 12b based on open-source files of [19], which consists of a 3-D Van Atta array (VAA) antenna and 16 PIN diodes [20]. The sync-control board of h-tag is identical to that of m-tag. The power consumption of h-tag is around 1920 $\mu$ W (570 $\mu$ W from the sync-control board and 1350 $\mu$ W from the diodes). h-Tag has 19dBi VAA antenna gain and a wide radiation coverage of 90° and 140° in azimuth and elevation planes. Such wide coverage motivates us to use h-tag in 2-D and 3-D experiments.

**Radar.** Most experiments use an ADI TinyRad [14] radar operating at 24GHz-24.25GHz. In experiments involving multiple radars, an Infineon Position2Go [21] radar operating at the same frequency band is also used. The sampled IF signal collected by the radar is conveyed to a ThinkPad X1 [22] laptop, which executes the demodulation technique.

## 5.2 Main Results

We evaluate the performance of Serena by experiments carried out in 1-D, 2-D, and 3-D space, respectively.

**5.2.1 Experiments in 1-D Space.** The setup and result of 1-D experiments for evaluating Serena are as follows.

**Setup.** The experiments are conducted in an indoor corridor and outdoor roadway in Fig. 13a. In each environment, we deploy an m-tag which adopts HDD modulation, and set  $\Delta f$  to be an integer times the frequency resolution of radar IF spectrum. As such integer affects SSR, it is hereafter referred to as *SSR constant (SC)*. We conduct experiments with  $SC \in \{1, 8, 32\}$ . Under each SC, we divide 1-D space into multiple cells, and vary the distance between the tested radar location and tag from 5m to 24m in 0.5m increment. For each tested location, we configure the tag to deliver symbols to the cell containing it and record the in-cell BER, and also configure the tag to deliver symbols to other cells and record the average out-of-cell BER. The radar is set to directly face the tag with its antenna plane parallel to that of the tag.

**Result.** Fig. 18 presents the in-cell BER of Serena in different environments, SCs, and SNRs, where SNR is defined as

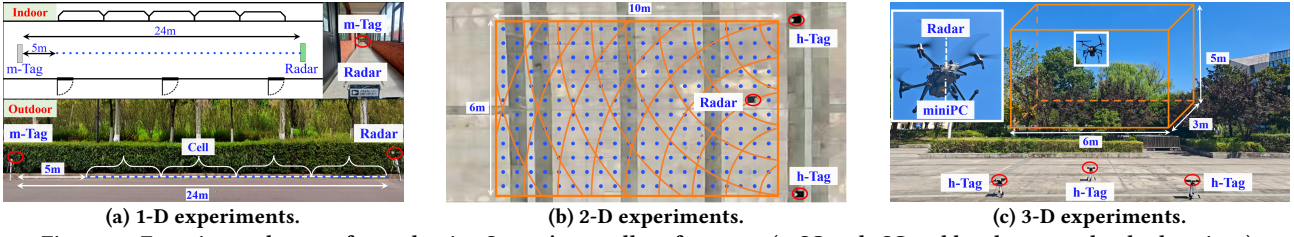


Figure 13: Experimental setups for evaluating Serena's overall performance (a: SC=8; b: SC=2; blue dots: tested radar locations).

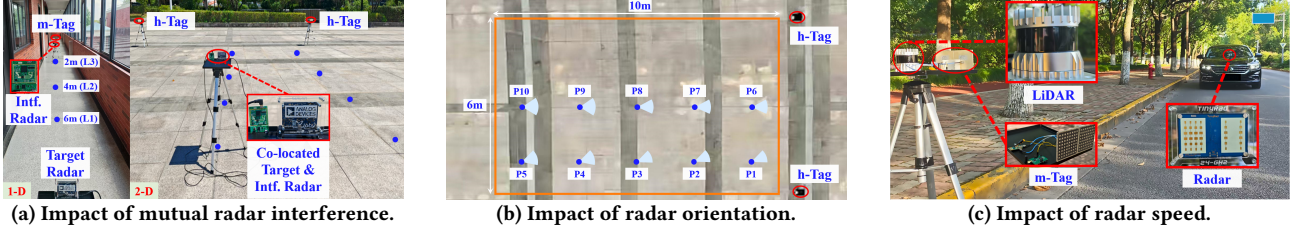


Figure 14: Experimental setups for evaluating impact of practical factors (blue dots: tested radar locations; circular sector: orientation range).

the ratio between harmonic power to the average power of the signal in other frequencies in IF spectrum after performing interference suppression when demodulation. Clearly, the in-cell BER decreases with SNR and SC. Such trend is attributed to two reasons. First, as illustrated in Fig. 19, higher SNR enhances the distinguishability of the tag-modulated harmonic, thereby reducing the demodulation errors. Second, larger SC corresponds to a larger frequency spacing between adjacent symbols, which reduces the chance of symbol misclassification. It is notable that the average in-cell BER is consistently less than 0.6% in both environments, whereas the out-of-cell BERs in all experiments across different environments are around 30% as shown in Fig. 20.

**5.2.2 Experiments in 2-D Space.** The setup and result of 2-D experiments for evaluating Serena are as follows.

**Setup.** Fig. 13b illustrates the setup of evaluating Serena in 2-D space. Specifically, we conduct two sets of experiments. In the first set of experiments, we deploy two h-tags separated by 6m, and set the testing area as a 10m×6m area in the intersection of tags' radiation coverage. We evenly separate the testing area into 0.5m×0.5m grids. The centers of all the grids are the tested radar locations. The tags performs HDD modulation under  $\text{SC} \in \{1, 2, 8\}$ . Similar to the setup in § 5.2.1, under each SC, we measure the in-cell and out-of-cell BER of each tested location. In the second set of experiments, we deploy an additional h-tag at the middle point between the above two tags, and measure the in-cell and out-of-cell BER with the three tags adopting HDD modulation with  $\text{SC} = 1$ . We set the radar's antenna plane to be parallel to the line connecting the tags in both sets of experiments.

**Result.** Fig. 15 illustrates Serena's in-cell BER map in 2-D experiments with the tested locations centered at the grids and the color of each grid representing the in-cell BER of the tested location that it contains. Fig. 15 shows that (i)

given SC and number of tags, the in-cell BER increases with the distances between the radar and the tags, (ii) given the number of tags, the BER at the same tested location decreases with SC, and (iii) given  $\text{SC} = 1$ , the in-cell BER with 2 tags is lower than that with 3 tags. Specifically, (i) holds because larger radar-tag distance leads to lower SNR of tag signals, (ii) holds because larger SC indicates larger margin between the adjacent symbol-representing frequencies, and (iii) holds because correct demodulation requires to correctly recognize the harmonics generated by all tags. Fig. 21a illustrates the impact of tag's min and mean SNR, SC, and the number of tags on in-cell BER in quantification, and shows similar trends as indicated by Fig. 15. Clearly, Serena achieves less than 0.9% average in-cell BER in all the 2-D experiments. Besides, as illustrated in Fig. 21b, Serena's out-of-band BER is around 30% in all the experiments.

**5.2.3 Experiments in 3-D Space.** The setup and result of 3-D experiments for evaluating Serena are as follows.

**Setup.** Fig. 13c illustrates the setup of evaluating Serena in 3-D space. Specifically, we place three h-tags on the ground facing the sky, and set the testing space as a 3m×6m×5m space in the intersection of tags' radiation coverage. We evenly separate the testing space into 1m×1m×1m cubes. The centers of the cubes are the tested radar locations. We equip the radar on a DJI Matrice 210 [23] UAV, and let the UAV hover at each tested location. An Intel NUC 11 [24] miniPC on the UAV is connected with the radar to supply its power and execute the demodulation technique. We conduct experiments with the tags performing HDD modulation under  $\text{SC} \in \{1, 2, 4\}$ . Under each SC, we measure the in-cell and out-of-cell BER of each tested location. The radar's antenna plane is parallel to those of the tags.

**Result.** Fig. 16 illustrates Serena's in-cell BER map in 3-D experiments. Specifically, given SC, each image in Fig. 16

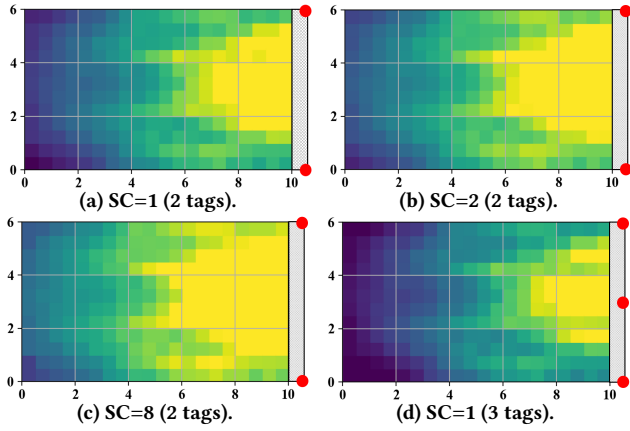


Figure 15: In-cell BER map in 2-D experiments (brighter grid: lower BER; red dot: tag location; unit: m).

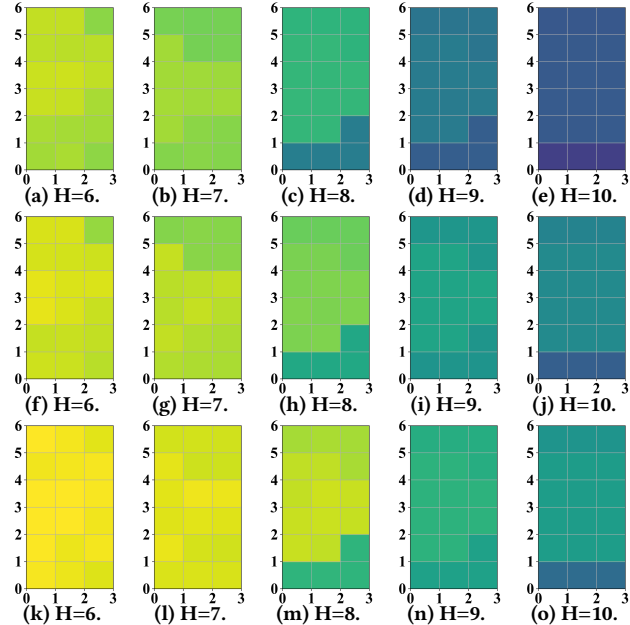


Figure 16: In-cell BER map in 3-D experiments (H: UAV height; unit: m; 1st row: SC=1; 2nd row: SC=2; 3rd row: SC=4).

corresponds to BER map of a specific height with the center of each grid in the image representing the tested location at such height and the color of grids representing the in-cell BER. From Fig. 16, we draw similar findings as those in Fig. 15: shorter radar-tag distance and smaller SC lead to lower in-cell BER. Fig. 22a illustrates the impact of tag's min and mean SNR, SC, and the number of tags on in-cell BER. Clearly, Serena achieves less than 1% average in-cell BER in all 3-D experiments. Besides, as shown in Fig. 22b, Serena's out-of-band BER is higher than 22% in all the experiments.

**5.2.4 Data Rate.** The data rate of Serena is jointly decided by the number of tags  $X$ , the interval  $\Delta f$  between adjacent symbol-representing harmonic frequencies, as well as other

Table 1: Serena's average cell size (1-D:  $m$ ; 2-D:  $m^2$ ; 3-D:  $m^3$ ).

Exp.	1-D Experiments			2-D Experiments			3-D Experiments			
(X, SC)	(1, 1)	(1, 8)	(1, 32)	(2, 1)	(2, 2)	(2, 8)	(3, 1)	(3, 2)	(3, 4)	
Cell Size	0.6	4.8	19.2	0.38	1.18	6.94	0.21	0.36	1.13	3.84

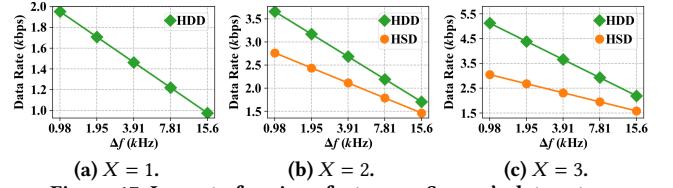


Figure 17: Impact of various factors on Serena's data rate.

parameters including  $f_{\max}$ ,  $R_{\max}$ , and chirp duration  $T_c$ . Serena sets  $f_{\max} = 500\text{kHz}$ ,  $R_{\max} = 30\text{m}$ , and  $T_c = 1024\mu\text{s}$ . The data rates under different  $X$  and  $\Delta f$  are shown in Fig. 17. Clearly, larger  $X$  and smaller  $\Delta f$  lead to higher data rate by enlarging the number of symbols. Besides, Serena achieves more than 1kbps data rate under most  $X$  and  $\Delta f$  values, which is sufficient to convey byte-level notification messages to radar-equipped vehicles within  $ms$ -level duration.

Fig. 17 compares the data rate of HDD modulation with a baseline method, harmonic-sharing distributed (HSD) modulation, that allows multiple tags to share symbol-representing harmonic frequencies. Specifically, HSD modulation allocates exclusive modulation durations to tags, such that the radar can distinguish the harmonics generated by different tags based on their different modulation timings. As shown in Fig. 17, with the same per-tag modulation duration and inter-symbol idle duration, HDD modulation achieves higher data rate than HSD when  $X \geq 2$ . This is contributed by HDD's shorter symbol modulation time, as it enables multiple tags to modulate concurrently to deliver a symbol. Note that HDD and HSD modulation are equivalent when  $X = 1$ .

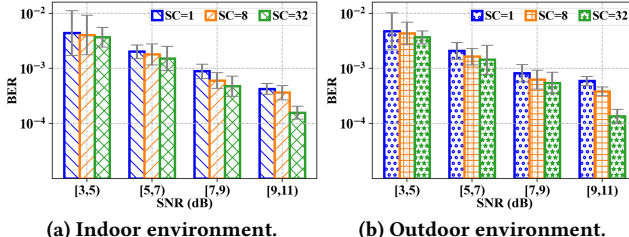
**5.2.5 Spatially Selective Resolution.** As illustrated in § 3.4, the SSR of Serena is jointly impacted by  $X$  and  $\Delta f$  (or equivalently SC). In Tab. 1, we present the SSR of Serena in the previous experiments by demonstrating the average sizes of the cells. Note that beyond the values in the table, Serena can further enlarge the cell size by enlarging SC, or reduce the cell size by enlarging  $X$ .

### 5.3 Impact of Practical Factors

**5.3.1 Impact of Radar Mutual Interference.** The setup and result under radar mutual interference are as follows.

**Setup.** In practice, multiple vehicles could operate within the same area, which leads to mutual interference among the radars deployed on them. We conduct experiments to evaluate the impact of radar mutual interference on Serena in 1-D and 2-D spaces with the following setups.

**1-D Space.** The environment, tag type and placement of this experiment are identical to those in § 5.2.1. As shown in Fig. 14a, we place the radar that transmits interference



(a) Indoor environment.

Figure 18: In-cell BER in 1-D experiments.

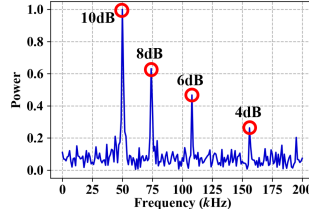


Figure 19: Harmonic SNR.

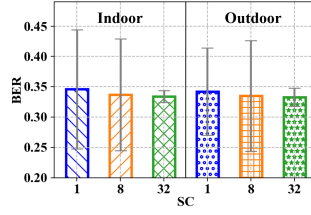


Figure 20: 1-D out-of-cell BER.

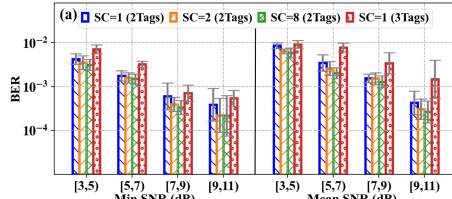


Figure 21: In cell (a) and out-of-cell (b) BER in 2-D experiments.

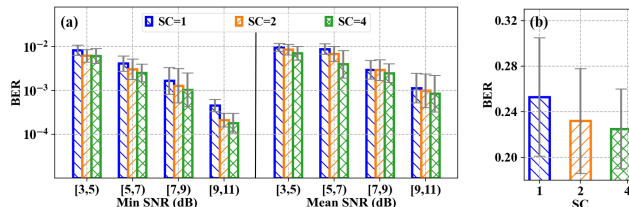


Figure 22: In-cell (a) and out-of-cell (b) BER in 3-D experiments.

signals on the line connecting the tag and the radar at the target location. Such placement maximizes the radar interference in 1-D space by ensuring that the signals transmitted by the interference radar and modulated by the tag can be received by the target radar. We set the distance between the target radar and the tag as 10m, and that between the interference radar and the tag as 6m, 4m, and 2m to generate three interference levels L1, L2, and L3. We also evaluate Serena in no-interference scenario, where the interference radar is turned off. We conduct two sets of experiments, where TinyRad and Position2Go are respectively used as the target radar, while the other served as the interference radar.

**2-D Space.** The environment, tag type and placement of this experiment are identical to those in § 5.3.2. As shown in Fig. 14a, we place the target and interference radar at the same location. Such placement maximizes the radar interference in 2-D space by ensuring the signals transmitted by the interference radar and modulated by the tag can be received by the target radar. We conduct two sets of experiments, where TinyRad and Position2Go are respectively the

Table 2: In-cell BER in 1-D experiments for impact of radar mutual interference (NI: no radar mutual interference; unit: %).

Target Radar Interference	TinyRad				Position2Go			
	NI	L1	L2	L3	NI	L1	L2	L3
BER	0.058	0.06	0.061	0.065	0.082	0.082	0.085	0.085

Table 3: In-cell BER in 2-D experiments for impact of radar mutual interference (I: with radar mutual interference; unit: %).

Radar	TinyRad								
	Location	P1	P2	P3	P4	P6	P7	P8	P9
BER (NI)	0.002	0.008	0.02	0.32	0.001	0.004	0.046	0.19	
BER (I)	0.002	0.012	0.022	0.32	0.001	0.004	0.052	0.21	
Radar	Position2Go								
	Location	P1	P1	P3	P4	P6	P7	P8	P9
BER (NI)	0.004	0.007	0.055	0.038	0.004	0.008	0.062	0.35	
BER (I)	0.005	0.011	0.058	0.04	0.004	0.012	0.063	0.35	

target radar. The tested radar locations are P1-P4 and P6-P9 in Fig. 14b. We do not test on P5 and P10, where Position2Go performs poorly even under no interference due to low SNR.

**Result.** Tab. 2 shows the in-cell BER obtained in 1-D experiments under different interference levels. Clearly, radar mutual interference has minor impact on BER. Tab. 3 shows that in 2-D experiments the in-cell BER with mutual interference is similar to that without interference for both radars at all the tested locations. In all experiments, the out-of-cell BERs at all tested locations are larger than 31%. Such results validate the resilience of Serena on radar mutual interference. In fact, radar mutual interference would influence the demodulation only if the difference between the time that the target radar begins to transmit a chirp and that it receives the interference signal does not exceed several  $\mu$ s, which seldom happens in practice.

**5.3.2 Impact of Radar Orientation.** The setup and result for evaluation under varying radar orientation are as follows.

**Setup.** As illustrated in Fig. 14b, we select 10 tested radar locations (denoted as P1-P10) evenly distributed in the middle and right side of the testing area of the 2-D experiments in § 5.2.2. We do not select the locations on the left side of this area, because they are symmetric to P1-P5. At each tested location, we configure the tags to deliver symbols to the cell containing it, as well as other cells in the testing area. We change the orientation of the radar placed at each tested location in  $10^\circ$  increments until one of the tags falls outside its field of view (FoV). The experiments are conducted with the two tags adopting HDD modulation under  $SC \in \{1, 2, 8\}$ .

**Result.** Fig. 23 illustrates the in-cell BER when the radar is at P1-P10 under varying radar orientations. Generally, as long as both tags are in the radar's FoV, the orientation of the radar has only minor impact on in-cell BER. Besides, in all experiments, the out-of-cell BERs at all tested locations are larger than 27%. Such result validates Serena's robustness to radar orientation, which benefits from the wide FoV of around  $80^\circ$  of the tested radar. Thus, Serena's robustness to radar orientation also holds in 1-D and 3-D spaces.

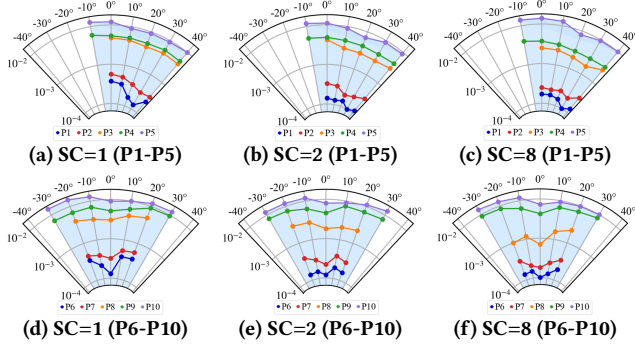


Figure 23: Impact of radar orientation.

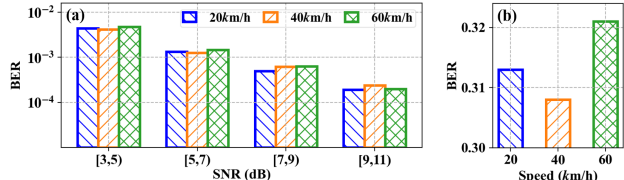


Figure 24: Impact of radar speed on in-cell (a) and out-of-cell (b) BER.

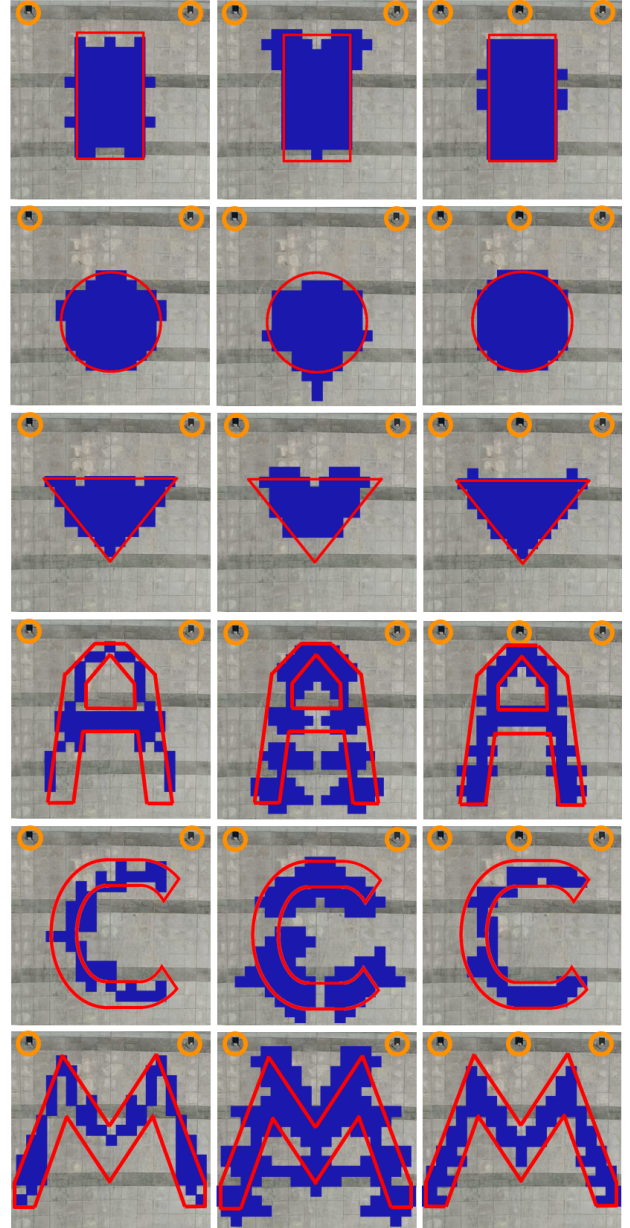
**5.3.3 Impact of Radar Speed.** The setup and result for evaluation under varying radar speed are presented as follows.

**Setup.** As illustrated in Fig 14c, we attach the radar on a Volkswagen [25] automobile, which moves at three levels of speeds, i.e., 20km/h, 40km/h, and 60km/h in three sets of experiments, respectively. We deploy an m-tag on the roadside, and set the testing space as the segment of the roadway with 5m to 24m distances to the tag. The tag adopts HDD modulation with  $SC = 8$ . At each automobile speed, an experiment is conducted for each cell in the testing space, where the tag delivers symbols to that cell and the automobile traverses the entire testing space. An Ouster [26] LiDAR is used to obtain the ground truth of automobile location.

**Result.** Fig. 24 shows Serena's average in-cell and out-of-cell BER under different automobile speeds. Clearly, Serena achieves a low in-cell BER of less than 0.7%, and an out-of-cell BER of around 30%, across all the experiments. Besides, given the SNR level, the automobile speed has minor impact on Serena's in-cell BER. In fact, even the vehicle speed reaches 60km/h, the induced 2.67kHz Doppler shift remains much smaller than the interval  $\Delta f = 15.6\text{kHz}$  between adjacent symbol-representing harmonic frequencies in the experiment, and thus has negligible impact on demodulation. It is worth noting that when delivering symbols to radars mounted on high-speed vehicles, SC should not be set too small to avoid demodulation errors caused by doppler shift.

#### 5.4 Serena-HDD<sup>+</sup> Evaluation

**Setup.** To evaluate Serena under HDD<sup>+</sup> modulation (referred to as Serena-HDD<sup>+</sup>), we deploy h-tags to deliver symbols to 2-D space with specific shapes, including rectangle, triangle, and square, as well as alphabetic letters 'A', 'C', and 'M'. We conduct three sets of experiments, including deploying two h-tags modulating with  $SC \in \{1, 2\}$ , and deploying

Figure 25: Serena-HDD<sup>+</sup> evaluation (1st column: 2 tags, SC=1; 2nd column: 2 tags, SC=2; 3rd column: 3 tags, SC=1; orange cycles: tags).

three h-tags modulating with  $SC = 1$ , respectively. We partition the 2-D space in front of the tags into  $0.3\text{m} \times 0.3\text{m}$  grids and measure the in-cell BER at the center of each grid. The realized communication region is defined as the collection of grids at whose centers the in-cell BERs are below 1%.

**Result.** Fig. 25 shows the target region inside the red lines, and fills the realized region in blue. Clearly, smaller SC and larger number of tags improves the similarity between the realized and target region. The rational behind such results lies in that smaller SC and larger tag number lead to a smaller cell size and enable a finer-grained fitting of the target region.

## 6 Related Work

**Backscatter Communication.** [1–7] devote themselves to develop radar backscatter communication systems, and have made promising achievements such as over 100m radar-tag communication distance [1], tens-of-GHz compatible spectrum range [2], designing fully passive tags [3], enabling two-way radar-tag communication [4, 5], supporting concurrent transmission from over 1000 tags to a radar [6], decreasing the interference between radar sensing and backscatter communication [7], and many others. Moreover, another set of backscatter communication systems [27–43] are developed for non-radar signals (e.g., WiFi, LoRa, visible light). Existing backscatter communication systems lack spatial selectivity, because the signal features that they use to represent symbols lack location specificity.

**Spatially Selective Communication.** Geocasting protocols [44–46] are among the most classic methods for spatially selective communication, which require the receiver to actively broadcast its location and the transmitter to check whether the receiver resides at the target location. Another set of methods [9–13] utilize range-selective beamforming to concentrate RF signal strength at target locations. These methods are inapplicable for radar backscatter, because they require to install power-intensive components (e.g., phase shifter, VCO) on tags which could consume 100mW- to W-level power. Note that there also exist acoustic-based methods [47, 48], which require either beamforming or power-intensive neural work inference, and thus their design philosophy are also inapplicable for low-power tags. Besides, such methods have less than 6m communication distance and thus are unsuitable for message delivery to vehicles.

**Tag Synchronization.** One set of works [34, 35] that aim to synchronize low-power backscatter tags rely on the device that generates tag carrier signal to also generate clock reference signal. However, to reliably detect the radar signal, a tag has to be equipped with 100mW-level always-on components (e.g., LNA), which are overly power consuming. Other sync methods could be applied for low-power tags exploit ambient signals (e.g., power line radiation [49], signal of dedicated radio transmitter [50, 51]) as reference signal, which typically only exist in specific environments.

**Radar Backscatter Sensing.** Another line of works focus on radar backscatter sensing, and have achieved 100m-level ranging [19, 52], none-line-of-sight sensing [53–55], radar detection [56], drone tracking [57, 58], and micro displacement measurement [59]. As they focus on sensing rather than communication, they are orthogonal to Serena.

## 7 Conclusion and Discussion

This paper presents Serena, the first system that enables spatially selective radar backscatter communication with

low-power tags. Our experimental results show that Serena achieves less than 1% average BER at target locations, while keeping the average BER around 30% at non-target locations. Serena offers a low-power solution for delivering location-specific messages to radar-equipped automobile, UAV, and UGV. We then discuss several practical issues and possible solutions when Serena faces real-world deployment.

**Over-the-Air Tag Configuration.** When target locations change, one could conveniently reconfigure the tags by reusing the sync radio of Serena as the receiver of over-the-air updated configuration messages. Such messages can be broadcast by a low-power radio equipped on a moving UAV or UGV, which flexibly approaches the vicinity of the tags and delivers the updated configuration messages.

**Communication Distance.** Serena currently has 24m maximum communication distance, which can be improved with two methods. The first method is chirp extension, which can be realized by directly extending the chirp duration or stitching multiple chirps as a super chirp [6]. We conduct an experiment that extends chirp duration from  $1024\mu s$  used in § 5.2 to  $8192\mu s$ , whose results show that Serena's maximum communication distance extends to 40m. However, chirp extension decreases data rate. The second method is to use antennas with higher gain. For example, the antenna in [60] offers 8dB more gain than the antenna of m-tag, which could theoretically double Serena's communication range.

**Radar Operating Frequency.** Serena's design principle is independent to the radar's operating frequencies. In fact, Serena can be seamlessly extended for radars operating at 60GHz or 77GHz by using the tags whose backscatter modules operating at these frequencies [2, 55], and integrating them with Serena's low-power sync radio.

**Interference with Radar Sensing.** Serena has minimal impact on the sensing functionality of radar. Specifically, the modulation scheme of Serena ensures that at least one out of every four chirps is unmodulated. Using those unmodulated chirps, the radar can reliably estimate target range and angle. A potential effect arises in velocity estimation, whose accuracy is proportional to the number of available chirps. Although Serena's modulation renders some chirps unusable for velocity estimation, its impact can be mitigated through super-resolution spectral estimation techniques [61].

**Multipath Interference.** Serena's demodulation technique makes it largely immune to multipath interference. Specifically, Serena selects the strongest harmonic within each tag's allocated frequency band during demodulation. Since the tag-modulated signals propagating along none-line-of-sight paths are weaker than that along the line-of-sight (LoS) path, their harmonics will not be selected. Besides, the narrow beam of m-tag could further suppress multipath interference, as it ensures that m-tag can only receive and reflect radar signal along the LoS path.

## References

- [1] E. Soltanaghai, A. Prabhakara, A. Balanuta, M. G. Anderson, J. M. Rabaeij, S. Kumar, and A. G. Rowe, "Millimetro: mmwave retro-reflective tags for accurate, long range localization," in *Proceedings of the 27th Annual International Conference on Mobile Computing and Networking, MobiCom*, 2021.
- [2] K. Qian, L. Yao, K. Zheng, X. Zhang, and T. N. T. Ng, "Uniscatter: a metamaterial backscatter tag for wideband joint communication and radar sensing," in *Proceedings of the 29th Annual International Conference on Mobile Computing and Networking, MobiCom*, 2023.
- [3] J. Nolan, K. Qian, and X. Zhang, "Ros: passive smart surface for roadside-to-vehicle communication," in *Proceedings of the ACM SIGCOMM Conference, SIGCOMM*, 2021.
- [4] R. Okubo, L. Jacobs, J. Wang, S. M. Bowers, and E. Soltanaghai, "Integrated two-way radar backscatter communication and sensing with low-power iot tags," in *Proceedings of the ACM SIGCOMM Conference, SIGCOMM*, 2024.
- [5] J. He, M. Tang, R. Okubo, D. Panchmia, and E. Soltanaghai, "Extended-range two-way radar backscatter communication with low-power iot tags," in *Proceedings of the 30th Annual International Conference on Mobile Computing and Networking, MobiCom*, 2024.
- [6] K. M. Bae, N. Ahn, Y. Chae, P. Pathak, S.-M. Sohn, and S. M. Kim, "Omniscatter: extreme sensitivity mmwave backscattering using commodity fmcw radar," in *Proceedings of the 20th Annual International Conference on Mobile Systems, Applications and Services, MobiSys*, 2022.
- [7] K. Qian and P. Pathak, "Toward spoofing-resilient and communication-integrated mmwave radar sensing," in *Proceedings of the 22nd Annual International Conference on Mobile Systems, MobiSys*, 2025.
- [8] "Millimeter Wave Radar Market Overview," <https://www.marketgrowthreports.com/market-reports/millimeter-wave-radar-market-113823>.
- [9] W. T. Li, C. Cui, X. T. Ye, X. W. Shi, and H. C. So, "Quasi-time-invariant 3-d focusing beampattern synthesis for conformal frequency diverse array," *IEEE Transactions on Antennas and Propagation*, vol. 68, no. 4, pp. 2684–2697, 2020.
- [10] A.-M. Yao, P. Rocca, W. Wu, A. Massa, and D.-G. Fang, "Synthesis of time-modulated frequency diverse arrays for short-range multi-focusing," *IEEE Journal of Selected Topics in Signal Processing*, vol. 11, no. 2, pp. 282–294, 2017.
- [11] Z. Ahmad, Z. Shi, and C. Zhou, "Time-variant focusing range-angle dependent beampattern synthesis by uniform circular frequency diverse array radar," *IET Radar, Sonar & Navigation*, vol. 15, no. 1, pp. 62–74, 2021.
- [12] Z. Ahmad, Z. Shi, C. Zhou, and Y. Gu, "Time-variant focused range-angle dependent beampattern synthesis by frequency diverse array radar," *IET Signal Processing*, vol. 14, no. 6, pp. 352–360, 2020.
- [13] Y.-Q. Yang, H. Wang, H.-Q. Wang, S.-Q. Gu, D.-L. Xu, and S.-L. Quan, "Optimization of sparse frequency diverse array with time-invariant spatial-focusing beampattern," *IEEE Antennas and Wireless Propagation Letters*, vol. 17, no. 2, pp. 351–354, 2018.
- [14] "TinyRad," <https://www.analog.com/cn/resources/evaluation-hardware-and-software/evaluation-boards-kits/EVAL-TinyRad.html>.
- [15] "ADL6010," <https://www.analog.com/en/products/adl6010.html>.
- [16] "nrf52832," <https://www.nordicsemi.com/Products/nRF52832>.
- [17] "ADRFS026," <https://www.analog.com/en/products/adrfs026.html>.
- [18] "STM32L467RG," <https://www.st.com/en/microcontrollers-microprocessors/stm32l467rg.html>.
- [19] K. Bae, H. Moon, S. Sohn, and S. M. Kim, "Hawkeye: Hectometer-range subcentimeter localization for large-scale mmwave backscatter," in *Proceedings of the 21st Annual International Conference on Mobile Systems, Applications and Services, MobiSys*, 2023.
- [20] "MADP-000907-14020," <https://www.macom.com/products/product-detail/MADP-000907-14020P>.
- [21] "position2go," <https://www.mouser.com/new/infineon/Infineon-position2go-dev-kit>.
- [22] "Thinkpad X1 Carbon," <https://www.lenovo.com/us/en/d/thinkpad-x1-carbon/>.
- [23] "Matrice 210 user manual," [https://dl.djicdn.com/downloads/M200/20201120/M200\\_User\\_Manual\\_EN\\_20201120.pdf](https://dl.djicdn.com/downloads/M200/20201120/M200_User_Manual_EN_20201120.pdf).
- [24] "Intel NUC 11," <https://ark.intel.com/content/www/us/en/ark/products/121572/intel-nuc-11-pro-kit-nuc11tnhi30z.html>.
- [25] Volkswagen, "Volkswagen passat sedan," <https://www.volkswagen.com.au/en/models/passat.html>.
- [26] Ouster, <https://ouster.com/products/scanning-lidar/os1-sensor/>.
- [27] X. Guo, L. Shangguan, Y. He, N. Jing, J. Zhang, H. Jiang, and Y. Liu, "Saiyan: Design and implementation of a low-power demodulator for lora backscatter systems," in *Proceedings of the 19th USENIX Symposium on Networked Systems Design and Implementation, NSDI*, 2022.
- [28] Y. Song, L. Lu, J. Wang, C. Zhang, H. Zheng, S. Yang, J. Han, and J. Li, " $\mu$ mote: Enabling passive chirp de-spreading and  $\mu$ w-level long-range downlink for backscatter devices," in *Proceedings of the 20th USENIX Symposium on Networked Systems Design and Implementation, NSDI*, 2023.
- [29] S. Li, H. Zheng, C. Zhang, Y. Song, S. Yang, M. Chen, L. Lu, and M. Li, "Passive DSSS: empowering the downlink communication for backscatter systems," in *Proceedings of the 19th USENIX Symposium on Networked Systems Design and Implementation, NSDI*, 2022.
- [30] H. Lu, M. Mazaheri, R. Rezvani, and O. Abari, "A millimeter wave backscatter network for two-way communication and localization," in *Proceedings of the ACM SIGCOMM Conference, SIGCOMM*, 2023.
- [31] M. H. Mazaheri, A. Chen, and O. Abari, "mmtag: a millimeter wave backscatter network," in *Proceedings of the ACM SIGCOMM Conference, SIGCOMM*, 2021.
- [32] Y. Chae, Z. Lin, K. Bae, S. M. Kim, and P. Pathak, "mmcomb: High-speed mmwave commodity wifi backscatter," in *Proceedings of the 21st USENIX Symposium on Networked Systems Design and Implementation, NSDI*, 2024.
- [33] Q. Qin, K. Chen, Y. Xie, H. Luo, D. Fang, and X. Chen, "Pushing the throughput limit of ofdm-based wi-fi backscatter communication," in *Proceedings of the 30th Annual International Conference on Mobile Computing and Networking, MobiCom*, 2024.
- [34] M. Dunna, M. Meng, P. Wang, C. Zhang, P. P. Mercier, and D. Bharadia, "Syncscatter: Enabling wifi like synchronization and range for wifi backscatter communication," in *Proceedings of the 18th USENIX Symposium on Networked Systems Design and Implementation, NSDI*, 2021.
- [35] R. Zhao, F. Zhu, Y. Feng, S. Peng, X. Tian, H. Yu, and X. Wang, "Ofdma-enabled wi-fi backscatter," in *Proceedings of the 25th Annual International Conference on Mobile Computing and Networking, MobiCom*, 2019.
- [36] C. Du, J. Yu, R. Zhang, J. Ren, and J. An, "Orthcatter: High-throughput in-band OFDM backscatter with over-the-air code division," in *Proceedings of the 21st USENIX Symposium on Networked Systems Design and Implementation, NSDI*, 2024.
- [37] W. Akbar, A. Allam, and F. Adib, "The underwater backscatter channel: Theory, link budget, and experimental validation," in *Proceedings of the 29th Annual International Conference on Mobile Computing and Networking, MobiCom*, 2023.
- [38] A. Eid, J. Rademacher, W. Akbar, P. Wang, A. Allam, and F. Adib, "Enabling long-range underwater backscatter via van atta acoustic networks," in *Proceedings of the ACM SIGCOMM Conference, SIGCOMM*, 2023.

- [39] W. Wang, Y. He, Y. Xie, C. Xie, Y. Kai, and C. Hu, "Acoustic backscatter network for vehicle body-in-white," in *Proceedings of the ACM SIGCOMM Conference, SIGCOMM*, 2025.
- [40] K. Xu, C. Gong, B. Liang, Y. Wu, B. Di, L. Song, and C. Xu, "Low-latency visible light backscatter networking with retromumimo," in *Proceedings of the 20th ACM Conference on Embedded Networked Sensor Systems, SenSys*, 2022.
- [41] Y. Wu, P. Wang, K. Xu, L. Feng, and C. Xu, "Turboboosting visible light backscatter communication," in *Proceedings of the ACM SIGCOMM Conference, SIGCOMM*, 2020.
- [42] X. Xu, Y. Shen, J. Yang, C. Xu, G. Shen, G. Chen, and Y. Ni, "Passivevlc: Enabling practical visible light backscatter communication for battery-free iot applications," in *Proceedings of the 23rd Annual International Conference on Mobile Computing and Networking, MobiCom*, 2017.
- [43] A. Kludze and Y. Ghasempour, "Leakyscatter: A frequency-agile directional backscatter network above 100 ghz," in *Proceedings of the 20th USENIX Symposium on Networked Systems Design and Implementation, NSDI*, 2023.
- [44] J. C. Navas and T. Imielinski, "Geocast - geographic addressing and routing," in *Proceedings of the Third Annual ACM/IEEE International Conference on Mobile Computing and Networking, MobiCom*, 1997.
- [45] "GeoNetworking," [https://www.etsi.org/deliver/etsi\\_en/302600\\_302699/3026360401/01.02.01\\_30/en\\_3026360401v010201v.pdf](https://www.etsi.org/deliver/etsi_en/302600_302699/3026360401/01.02.01_30/en_3026360401v010201v.pdf).
- [46] P. Li, T. Zhang, C. Huang, X. Chen, and B. Fu, "Rsu-assisted geocast in vehicular ad hoc networks," *IEEE Wireless Communications*, vol. 24, no. 1, pp. 53–59, 2017.
- [47] W. Wang, Y. He, M. Jin, Y. Sun, and X. Guo, "Meta-speaker: Acoustic source projection by exploiting air nonlinearity," in *Proceedings of the 29th Annual International Conference on Mobile Computing and Networking, MobiCom*, 2023.
- [48] T. Fan, H. Wu, M. Jin, T. Chen, L. Shangguan, X. Wang, and C. Zhou, "Towards spatial selection transmission for low-end iot devices with spotsound," in *Proceedings of the 29th Annual International Conference on Mobile Computing and Networking, MobiCom*, 2023.
- [49] A. Rowe, V. Gupta, and R. Rajkumar, "Low-power clock synchronization using electromagnetic energy radiating from AC power lines," in *Proceedings of the 7th International Conference on Embedded Networked Sensor Systems, SenSys*, 2009.
- [50] Y. Chen, Q. Wang, M. Chang, and A. Terzis, "Ultra-low power time synchronization using passive radio receivers," in *Proceedings of the 10th ACM/IEEE International Conference on Information Processing in Sensor Networks, IPSN*, 2011.
- [51] J. Zhao, W. Gong, and J. Liu, "X-tandem: Towards multi-hop backscatter communication with commodity wifi," in *Proceedings of the 24th Annual International Conference on Mobile Computing and Networking, MobiCom*, 2018.
- [52] S. Mohan, K. Bansal, M. Dunna, and D. Bharadia, "Retroreflection with amplification for long range mmwave sensing," in *Proceedings of the 7th ACM Workshop on Millimeter-Wave and Terahertz Networks and Sensing Systems, mmNets*, 2023.
- [53] Z. Shi, Y. Yan, Y. Wang, W. Hu, and C. T. Chou, "N<sup>2</sup>los: Single-tag mmwave backscatter for robust non-line-of-sight localization," *arXiv*, 2025.
- [54] Y. Yan, Z. Shi, Y. Wang, C. Jiang, C. T. Chou, and W. Hu, "mmmiror: Device free mmwave indoor nlos localization using van-atta-array IRS," *arXiv*, 2025.
- [55] K. Bae, H. Moon, and S. M. Kim, "Supersight: Sub-cm NLOS localization for mmwave backscatter," in *Proceedings of the 22nd Annual International Conference on Mobile Systems, MobiSys*, 2024.
- [56] M. Tang, J. He, R. Okubo, D. Panchmia, and E. Soltanaghai, "Identifying and positioning fmcw radars using passive low-power tags," in *Proceedings of the 31th Annual International Conference on Mobile Computing and Networking, MobiCom*, 2025.
- [57] M. Lam, L. Dodds, A. Eid, J. G. Hester, and F. Adib, "6d self-localization of drones using a single millimeter-wave backscatter anchor," in *Proceedings of the IEEE Conference on Computer Communications, INFOCOM*, 2025.
- [58] S. Harisha, J. G. D. Hester, and A. Eid, "Dragonfly: Single mmwave radar 3d localization of highly dynamic tags in gps-denied environments," *arXiv*, 2025.
- [59] T. H. King, J. He, C. Yao, A. Prabhakara, M. Alipour, S. Kumar, A. Rowe, and E. Soltanaghai, "Platypus: Sub-mm micro-displacement sensing with passive millimeter-wave tags as "phase carriers"," in *Proceedings of the 22nd International Conference on Information Processing in Sensor Networks, IPSN*, 2023.
- [60] L. Zhang, Y. P. Zhang, and Y. Lu, "30-dbi gain microstrip grid array antenna at 24 ghz on a single-layer substrate," in *Proceedings of Antennas and Propagation Society International Symposium, APSURSI*, 2013.
- [61] R. Schmidt, "Multiple emitter location and signal parameter estimation," *IEEE Transactions on antennas and propagation*, vol. 34, no. 3, pp. 276–280, 1986.

## A Rationales of Location Specificity and Tag Controllability Mentioned in § 2

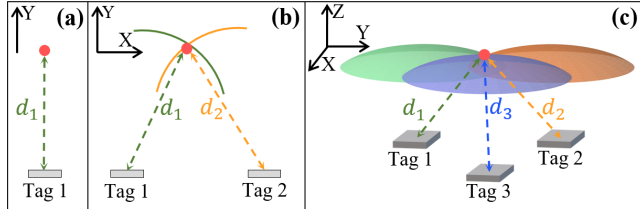


**Figure 26: Illustration of the uniqueness of the combination of the  $K$  distances between a location and the  $K$  tags in (a) 1-D, (b) 2-D, and (c) 3-D space, where  $d_i$  is the distance from the location represented by the red point to tag  $i$  with  $i \in \{1, 2, 3\}$ .**

The location specificity property mentioned in § 2 holds for two reasons: (i) in  $K$ -dimensional space within tags' radiation area, the combination of the  $K$  distances from a location to the  $K$  tags is unique; (ii) these distances uniquely determine the harmonic frequencies of the tags according to Eq. (1). Here, we illustrate (i) by discussing the following cases with  $K = 1, 2$ , or  $3$ , respectively.

**Case 1 ( $K = 1$ ).** As illustrated in Fig. 26a, in a 1-D space where the radar lies along a line with a tag at one endpoint, it is obvious that each location on the line corresponds to a unique distance to the tag.

**Case 2 ( $K = 2$ ).** As illustrated in Fig. 26b, a location in a 2-D space, whose distances to tag 1 and tag 2 are respectively  $d_1$  and  $d_2$ , is the intersecting point of 2 circles, one centered at tag 1 with radius  $d_1$  and the other centered at tag 2 with radius  $d_2$ . Such intersecting point is unique in the common radiation area of the tags. Besides, it is obvious that each location in a 2-D space corresponds to only one combination of distances to the 2 tags.

**Case 3 ( $K = 3$ ).** As illustrated in Fig. 26c, similar to the  $K = 2$  case, in the common radiation area of 3 tags in a 3-D space, a location with given distances  $d_1$ ,  $d_2$ , and  $d_3$  to the 3 tags is the unique intersecting point of 3 spheres, each centered at tag  $i$  with radius  $d_i$  where  $i \in \{1, 2, 3\}$ . Furthermore, each location in a 3-D space corresponds to only one combination of distances to the 3 tags.

The tag controllability property holds, because the harmonic frequency generated by each tag is influenced by its modulation frequency according to Eq. (1).

## B Exceptional Case in Demodulation

As illustrated in Fig. 27, the exceptional case occurs when the tag consecutively deliver the same symbol. In such case, the step 1 of the HDD demodulation technique will select multiple consecutive chirps for demodulation. We deal with such case by utilizing the fact that the first selected chirp  $j$  is integrally modulated, and thus the subsequent chirps  $\{j+4N : N \in \mathbb{N}^+\}$  are also integrally modulated. We preserve

the symbol classification results of the integrally modulated chirps, and discard the results of other chirps.

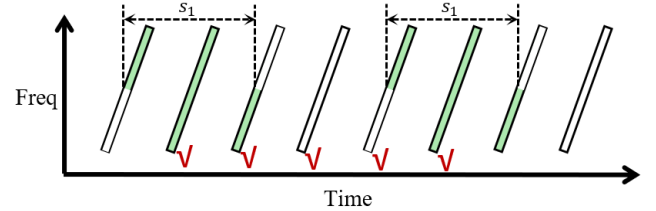


**Figure 27: Illustration of the exceptional case for HDD demodulation (symbol  $s_1$  is consecutively delivered by the tags twice).**